Controlled hydrodynamic conditions on the formation of iron oxide nanostructures synthesized by electrochemical anodization: effect of the electrode rotation speed.

Bianca Lucas-Granados, Rita Sánchez-Tovar, Ramón M. Fernández-Domene, Jose García-Antón*

Ingeniería Electroquímica y Corrosión (IEC). Instituto Universitario de Seguridad Industrial, Radiofísica y Medioambiental (ISIRYM). Universitat Politècnica de València. Camino de Vera s/n, 46022 Valencia, Spain.

** jgarciaa@iqn.upv.es*

Abstract

Iron oxide nanostructures are of particular interest because they can be used as photocatalysts in water splitting due to their advantageous properties. Electrochemical anodization is one of the best techniques to synthesize nanostructures directly on the metal substrate (direct back contact). In the present study, a novel methodology consisting of the anodization of iron under hydrodynamic conditions is carried out in order to obtain mainly hematite (α-Fe_2O_3) nanostructures to be used as photocatalysts for photoelectrochemical water splitting applications. Different rotation speeds were studied with the aim of evaluating the obtained nanostructures and determining the most attractive operational conditions. The synthesized nanostructures were characterized by means of Raman spectroscopy, Field Emission Scanning Electron Microscopy, photoelectrochemical water splitting, stability against photocorrosion tests, Mott-Schottky analysis, Electrochemical Impedance Spectroscopy (EIS) and band gap

measurements. The results showed that the highest photocurrent densities for photoelectrochemical water splitting were achieved for the nanostructure synthesized at 1000 rpm which corresponds to a nanotubular structure reaching ~0.130 mA · cm^{-2} at 0.54 V (vs. Ag/AgCl). This is in agreement with the EIS measurements and Mott-Schottky analysis which showed the lowest resistances and the corresponding donor density values, respectively, for the nanostructure anodized at 1000 rpm.

Keywords: iron oxide, nanostructure, hydrodynamic conditions, photocatalyst, water splitting.

1. Introduction

Iron oxide nanostructures are promising materials as photocatalysts in different applications such as wastewater treatment [1], gas detection [2], dye sensitized solar cells [3], degradation of organic dye pollutants [4], biomedicine [5], lithium batteries [6] and hydrogen generation [7]. Particularly, hematite (α-Fe_2O_3) is an attractive oxide form for photoelectrochemical water splitting to convert solar energy into clean and renewable hydrogen fuel [8]. Hematite is the most thermodynamically stable and the most common crystalline structure of the iron oxide under ambient conditions [9,10]. Besides, its band gap (~2.1 eV) is suitable for visible light absorption (up to ~590 nm). Additionally, its excellent chemical stability, non-toxicity and low cost make hematite be a proper material for photocatalytic applications. However, its efficiency is limited by several factors such as poor conductivity, short hole diffusion lengths (2-4 nm) and short lifetime of the excited-state carriers (10^{-12} s) [10–23]. In order to overcome these drawbacks different efforts have been focused on nanostructuring the material by electrochemical anodization, which is a process that allows synthesizing different

nanostructures directly on the metal substrate (i.e. direct back contact). This method significantly reduces the contact resistance between the nanostructure and the substrate, so the material can be directly used as a photocatalyst avoiding additional processes to join the nanostructure to the metal substrate, which in turn introduces an extra contact resistance to the photocatalyst [13,17,24,25].

Most of the studies related to iron anodization have been carried out under static conditions [24,26–30]. However, some authors studied the influence of stirring the electrolyte with a magnet during anodization in order to improve the diffusion process [17,31]. Nevertheless, in the present work a novel methodology is carried out, that is, stirring the iron rod under a controlled rotation speed during anodization. In this way, on the one hand, the diffusion process is enhanced and, on the other hand preferential paths are avoided. Furthermore, by controlling the rotation speed of the electrode during anodization, different nanostructures can be obtained. In previous works, the effect of controlled hydrodynamic conditions while stirring titanium, tungsten or zinc rods during anodization was evaluated achieving interesting and efficient nanostructures [32–34]. However, there is no literature concerning iron anodization under hydrodynamic conditions with a rotating anode.

In this study, the effect of controlled hydrodynamic conditions on iron anodization is evaluated. Different rotation speeds of the anode (iron metal) were tested in order to study the synthesized iron oxide nanostructures and determine the most suitable rotation speed in the studied range for obtaining an efficient photocatalyst. The morphology, electrochemical and photoelectrochemical properties of the nanostructures o

btained at the different hydrodynamic conditions were characterized by different methods such as Raman spectroscopy, Field Emission Scanning Electron Microscopy

(FE-SEM), photocurrent density vs. potential measurements (photoelectrochemical water splitting), stability against photocorrosion tests, Mott-Schottky (MS) analysis, Electrochemical Impedance Spectroscopy (EIS), and band gap measurements.

2. Experimental

2.1. Electrochemical anodization and annealing treatment

Electrochemical anodization was carried out using 99.9 % pure iron rod of 9.5 mm in diameter (an area of 0.7 cm^2 was exposed to the electrolyte) as working electrode, and a platinum foil as counter electrode. Prior to anodization, the surface of the iron rod was abraded with 220 to 4000 silicon carbide (SiC) papers and degreased by sonication in ethanol for 2 minutes. After this, the samples were properly rinsed with distilled water and dried in a nitrogen stream.

The electrolyte for the anodization was an ethylene glycol (EG) solution containing 0.1 M ammonium fluoride (NH_4F) and 3 vol% H_2O. The anodization was performed at 50 V for 15 minutes, and the current density vs. time was continuously measured during the process. In order to evaluate the influence of the controlled hydrodynamic conditions during the anodization process, the iron rod (anode) was connected to a rotating disk electrode (RDE). This RDE is coupled to a motor controller with an accuracy of ± 1 rpm in order to monitor the hydrodynamic conditions of the process. Figure 1 shows an illustration of the electrode configuration during the electrochemical anodization. Different controlled rotation speeds were applied during the electrochemical anodization, i.e. 0, 1000, 2000 and 3000 rpm, which correspond to the

Reynolds numbers of 0, 165, 325 and 490, respectively. The equivalence of the rotation speed with the Reynolds number was calculated as shown in Eq. 1:

$$Re = \frac{\omega \cdot \rho \cdot r^2}{\mu} \qquad (Eq.1)$$

where, *Re* is the Reynolds number, ω is the angular velocity expressed in rad·s^{-1} ($\omega = 2 \cdot \pi \cdot f / 60$, where f is the rotation speed in rpm), ρ is the electrolyte density in g·cm^{-3}, r is the radius of the immersed electrode expressed in cm and μ is the dynamic viscosity of the electrolyte in g·cm^{-1}·s^{-1}.

Once the anodization was finished, the samples were properly washed with distilled water and dried in a nitrogen stream. Annealing of the as-anodized samples was performed in a tube furnace at 500 °C for 1 hour in argon atmosphere. The heating rate was 15 °C · min^{-1} and the samples were cooled within the furnace by natural convection [35].

2.2. Structural characterization

The samples were examined by means of Raman spectroscopy in order to evaluate their crystalline structure. A neon laser 632 nm with ~700 μW was used. Additionally, the morphological characterization of the samples was performed using FE-SEM with an extra high tension (EHT) of 3 kV.

2.3. Electrochemical and photoelectrochemical characterization

Different electrochemical and photoelectrochemical experiments were carried out, such as photocurrent density vs. potential measurements (photoelectrochemical water splitting), stability tests, Mott-Schottky analysis, EIS measurements and band gap measurements.

All the electrochemical and photoelectrochemical experiments were carried out in a three-electrode configuration using the iron oxide nanostructure as the working electrode, a platinum tip as the counter electrode and a silver/silver chloride (Ag/AgCl, 3 M KCl) as the reference electrode. The area of the nanostructure exposed to the test solution was 0.26 cm^2 and the measurements were conducted in a 1 M KOH solution using an Autolab PGSTAT302N potentiostat. The photoelectrochemical measurements were performed under simulated sunlight conditions AM 1.5 (100 $mW \cdot cm^{-2}$).

Photocurrent density vs. potential measurements were recorded by scanning the potential from -0.4 to +0.6 V (vs. Ag/AgCl) with a scan rate of 2 $mV \cdot s^{-1}$. The measurements of photocurrent density as a function of the applied potential were recorded by chopped light irradiation (i.e. 0.02 V in the dark and 0.02 V in the light). The potentials measured vs. Ag/AgCl were converted to the reversible hydrogen electrode (RHE) scale according to the Nernst equation (Eq. 2) [14,36,37]:

$$E_{RHE} = E_{Ag/AgCl} + 0.059 \cdot pH + E^0_{Ag/AgCl} \qquad (\boldsymbol{Eq.2})$$

where E_{RHE} is the calculated potential (vs. RHE), $E_{Ag/AgCl}$ is the measured potential (vs. Ag/AgCl), pH is 14 for the prepared 1 M KOH solution and $E^0_{Ag/AgCl}$ is 0.207 V at a temperature of 25 ^oC for the used reference electrode.

MS plots, in dark and light conditions, were obtained in a 1 M KOH solution by sweeping the potential from the Open Circuit Potential (OCP) value (i.e. ~ - 0.3 V) in

the negative direction at 28 $mV \cdot s^{-1}$ with an amplitude signal of 0.01 V at a frequency value of 5 kHz. EIS measurements were performed in 1 M KOH at an applied potential of 0.35 V (vs. Ag/AgCl) in order to promote charge separation, and under both dark and light conditions over a frequency range from 100 kHz to 10 mHz with an amplitude of 0.01 V. Prior to each EIS test (for both dark and light conditions), samples were left at 0.35 V (vs. Ag/AgCl) in 1 M KOH solution for half an hour in order to stabilize them. For all the experiments performed under light conditions, simulated AM 1.5 illumination was used. Additionally, the samples were left in 1 M KOH at a potential of 0.35 V (vs. Ag/AgCl) under simulated light AM 1.5 (100 $mW \cdot cm^{-2}$) for 1 hour in order to verify their stability against photocorrosion.

The band gap measurements were performed in a 1 M KOH solution under potential-controlled conditions applying 0.35 V (vs. Ag/AgCl). The samples were irradiated by chopped light with a 300 W Xe Lamp in a wavelength range of 300 nm to 600 nm.

3. Results and discussion

3.1. Anodization under controlled hydrodynamic conditions

Figure 2 shows the evolution of the current density versus time during the anodization process of the different samples. There, three stages are clearly differentiated for all the nanostructures. In the first stage (I), the current density rapidly drops from approximately 80 $mA \cdot cm^{-2}$ to less than 15 $mA \cdot cm^{-2}$ in the case of the sample anodized in static conditions, and less than 25 in the ones anodized under hydrodynamic conditions. This quick decrease is due to the formation of a compact insulating oxide

layer (Fe_2O_3) on the iron substrate according to Eq. 3, and consequently, resistance increases immediately.

$$2Fe + 3H_2O \rightarrow Fe_2O_3 + 3H_2 \qquad (\boldsymbol{Eq.3})$$

The second stage (II) corresponds to a slight increase in the current density, which indicates that tiny pits occur in the surface of the compact layer followed by the formation of a nanoporous structure, resulting in resistance decrease. This process occurs because of the presence of the fluoride ions (F^-) and the high applied potential during anodization, which lead to a partial dissolution of the compact oxide layer, and a nanoporous structure is formed according to Eq. 4.

$$Fe_2O_3 + 12F^- + 6H^+ \rightarrow 2[FeF_6]^{3-} + 3H_2O \qquad (\boldsymbol{Eq.4})$$

The last stage (III) corresponds to further dissolution and cation-cation repulsion, then the nanoporous structure leads to a nanotubular one. At this point, current density remains almost constant because the equilibrium between the formation of the oxide layer and its chemical dissolution by F^- is reached, and then the formation of the tubular nanostructure stops [6,13,26,37].

According to Figure 2, for the nanostructure formed under static conditions (0 rpm) the current density values are lower in comparison to the ones synthesized under hydrodynamic conditions (1000, 2000 and 3000 rpm). In addition, current density increases with rotation speed, achieving their highest values for the samples anodized at 3000 rpm. This increase with the rotation speed is due to the fact that the steady-state current density is controlled by diffusion processes, so stirring the rods into the electrolyte increases the diffusion and hence, the current density is higher [38,39].

3.2. Raman spectroscopy

Figure 3 shows the Raman spectra of the samples anodized at different rotation speeds and annealed at 500 °C during 1 hour in argon atmosphere. After anodization, the formed iron oxide layer is amorphous, therefore, annealing is required in order to crystallize the structure and make the material suitable for being used as a photocatalyst [13,17,24,31]. Similar spectra were obtained for all the nanostructures, i.e. the same peaks appear at the same raman shifts, which means that there are no differences in the crystallinity of the samples regardless the hydrodynamic conditions used during anodization. The distribution of the peaks indicates that the nanostructures are mainly composed by hematite: 229 cm^{-1} (A_{1g}), 249 cm^{-1} (E_g), 295 cm^{-1} (E_g), 414 cm^{-1} (E_g), 500 cm^{-1} (A_{1g}), 615 cm^{-1} (E_g) and 1317 cm^{-1} (2nd order)[13]. However, some peaks also indicate the presence of magnetite in the nanostructures: 554 cm^{-1}, 672 cm^{-1} and ~ 820 cm^{-1} [40–44]. Thus, it can be concluded that the nanostructures obtained stirring the iron rod at the different rotation speeds are primarily composed by hematite with some amount of magnetite.

3.3. Field Emission Scanning Electron Microscopy

The morphology of the samples was evaluated by FE-SEM and Figure 4 shows the images acquired at different magnifications: 10000 X (a), c), e) and g)), and 30000 X (b), d), f) and h)). Figures 4 a) and b) correspond to the morphology of the samples anodized under static conditions (0 rpm). At this condition, a cracked porous initiation layer appears over the nanotubes, which partially covers the entrances of the real nanotubes. This undesirable initiation layer results in a decrease in the efficiency of the nanostructures as the nanotubes might be less accessible to light irradiation [45,46].

The morphology of the samples anodized at 1000 rpm is shown in Figures 4 c) and d). There, the initiation layer is etched and then, the entrances of the real nanotubes become more accessible. This makes the nanotubes more accessible to light irradiation and then, the photoactivity of the sample might be higher. Furthermore, nanotubular morphology is an advantageous geometry in order to improve the electron transport behavior, and avoid the short hole diffusion length problem since the route from the place of the generation of the holes to the surface where the oxidation reactions occur is shorter [25,47,48].

Figures 4 e) and f) show the samples anodized by stirring the iron rod at 2000 rpm. At this rotation speed the nanotubes collapse and seem to be stacked. Hence, the nanotubes are unseen and the top morphology seems to be chaotic. This might also affect the photoactivity of the samples as light irradiation can not go deep into the nanotubes.

Figures 4 g) and h) show that at a rotation speed of 3000 rpm, the morphology is a mixture between the morphology of the samples anodized at 0 and 2000 rpm, i.e. the nanotubes collapse and seem to be stacked though a porous initiation layer is also present in some parts of the nanostructure, covering the entrances of the nanotubes. This suggests that the photoactivity of the nanostructure may be affected by the two factors and the nanotubes can not perceive light irradiation. This could be due to the fact that at 3000 rpm the rotation speed is too high and some vortex can be formed, leading to anodization in non-homogeneous conditions.

On the other hand, Figure 5 shows that the rotation speed during the anodization does not affect the thickness of the nanostructures.

3.4. Photoelectrochemical water splitting

Figure 6 a) shows the water splitting performance under simulated sunlight AM 1.5 for the nanostructures synthesized at the different rotation speeds. The highest photocurrent density values were achieved for the sample anodized at 1000 rpm, indicating its suitability as photocatalyst for photoelectrochemical water splitting over the other ones. As the crystalline structure of all the samples is similar (see Raman spectra in Fig. 3), the differences in the achieved photocurrent densities are mainly attributed to their morphology. For instance, at 0.54 V (vs. Ag/AgCl) (the potential at which all the samples are stable during the water splitting tests), the highest photocurrent density corresponds to the sample anodized at 1000 rpm and it was ~0.130 mA · cm^{-2} (Figure 6 a)). This is related to the morphology of the sample anodized at 1000 rpm, which consists of a nanotube layer with the entrances of the tubes accessible to the light according to Figs. 4 c)-d). The nanotubular morphology is favorable for hematite as it reduces the recombination rate and promotes charge transport [9,13,47,49,50].

Figure 6 a) shows that the sample anodized at 2000 rpm achieved a photocurrent density of approximately ~0.090 mA · cm^{-2} at 0.54 V (vs. Ag/AgCl), which is lower than the one reached for the sample anodized at 1000 rpm. This is due to the collapsed and stacked nanotube layer obtained for the sample anodized by stirring the electrode at 2000 rpm (see Figs. 4 e)-f)). Then, this chaotic nanostructure where the nanotubes are less accessible to light irradiation increases recombination rate.

Finally, Figure 6 a) shows that the samples anodized at 0 and 3000 rpm reached similar photocurrent density values, i.e. ~0.065 mA · cm^{-2} and ~0.070 mA · cm^{-2}, respectively. These values are lower than those achieved for the nanostructures anodized at 1000 and 2000 rpm. For the sample anodized at 0 rpm the presence of a porous initiation layer covering the nanotubular structure (see. Figs. 4 a)-b)) suggests that the light is less accessible to the nanostructure and also the recombination rate is higher because of the

compact nature of the initiation layer. For the sample synthesized at 3000 rpm, an initiation layer and a collapsed and stacked nanotubular structure appears, as shown in Figs. 4 g)-h). Thus, this nanostructure is less accessible to light irradiation and the recombination rate is higher due to the combination of these two negative effects.

3.5. Stability against photocorrosion

The importance of verifying the stability of the prepared photocatalyst is due to the fact that commercial viability of photoelectrochemical hydrogen production requires long-term stable devices [51]. The nanostructures were left at 0.35 V (vs. Ag/AgCl) for 1 hour in the presence of light in order to verify their stability against photocorrosion. Figure 6 b) shows that the evolution of the photocurrent density vs. time remains constant for all the samples, which indicates that all the samples were stable against photocorrosion. Additionally, it is noteworthy that the photocurrent densities for the sample anodized at 1000 rpm are higher than those corresponding to the other nanostructures, which confirms the higher photoactivity of this sample. This is in agreement with the photoelectrochemical water splitting tests (Fig. 6 a)).

3.6. Mott-Schottky analysis

Figure 7 shows the MS plots under dark (a)) and light (b)) conditions in 1 M KOH for the samples anodized at the different rotation speeds. A positive slope corresponding to an n-type semiconductor behavior is observed for all the samples in both dark and light conditions [12]. The higher slopes of the linear region of the MS plots indicate a lower electron donor density according to the Mott-Schottky equation used for an n-type semiconductor [36,51–54]:

$$\frac{1}{{C_{SC}}^2} = \left(\frac{2}{e \cdot \varepsilon_0 \cdot \varepsilon_r \cdot N_D}\right) \cdot \left(E - E_{FB} - \frac{k \cdot T}{e}\right) \qquad (\boldsymbol{Eq.5})$$

where C_{SC} is the space charge layer capacitance, e the electron charge ($1.60 \cdot 10^{-19}$ C), ε_0 the vacuum permittivity ($8.85 \cdot 10^{-14}$ F $\cdot$ cm^{-1}), ε_r the dielectric constant (80 is the assumed value for the nanostructures [55,56]), N_D the donor density, E the applied potential, E_{FB} the flat-band potential, k the Boltzmann constant ($1.38 \cdot 10^{-23}$ J $\cdot$ K^{-1}) and T the absolute temperature.

The donor density, N_D, is calculated from the slopes (σ) of the linear regions of the MS plots as Eq. 6 indicates.

$$N_D = \left(\frac{2}{e \cdot \varepsilon_0 \cdot \varepsilon_r \cdot \sigma}\right) \qquad (\boldsymbol{Eq.6})$$

Table 1 shows the values of the donor density for the different nanostructures. The values are of the order of 10^{19} cm^{-3} regardless of the rotation speed applied to the electrode during anodization. Additionally, the values obtained under illumination are higher than under dark conditions for all the samples. This is because illumination generates electron-hole pairs and hence, the donor density increases. The samples anodized at 0 and 3000 rpm have the highest values of donor density under both dark ($3.98 \cdot 10^{19}$ cm^{-3} and $2.47 \cdot 10^{19}$ cm^{-3}, respectively) and light conditions ($14.35 \cdot 10^{19}$ cm^{-3} and $5.80 \cdot 10^{19}$ cm^{-3}, respectively), however they show the lowest photocurrent densities in the photoelectrochemical water splitting tests (Figure 6 a)). This is due to the fact that when the value of donor density is too high, part of these defects act as carrier traps (trapping electrons or holes) and then, the efficiency of the photocatalyst in the water splitting process is reduced [57]. Consequently, the samples with lower donor density values improve water splitting performance. The nanostructure synthesized at 1000 rpm, with donor densities of $1.02 \cdot 10^{19}$ cm^{-3} and $2.22 \cdot 10^{19}$ cm^{-3} in dark and light

conditions, respectively, achieve the highest photoresponse in the photoelectrochemical water splitting according to Fig. 6 a).

The flat-band potential (E_{FB}) is the potential at which there is no depleted space charge layer, i.e. it is the potential needed to be applied to the semiconductor in order to reduce band bending to zero. This flat-band potential is related to the applied external potential (E) and to the potential drop at the depletion space charge layer ($\Delta\phi_{SC}$), according to Eq. 7.

$$\Delta\phi_{SC} = E - E_{FB} \qquad (\boldsymbol{Eq.7})$$

For a constant applied external potential, higher and more negative flat-band potential results in higher potential drop at the depletion space charge layer. Consequently, the electrical field within the depleted space charge layer increases (i.e. the driving force to separate the generated electron-hole pairs) and hence, the recombination rate decreases [58].

The flat-band potential value is obtained from the intercept of the linear region of the MS plots with the x-axis. Table 1 shows E_{FB} values for the samples anodized at the different rotation speeds showing almost no differences (between -0.6 and -0.8 V (vs. Ag/AgCl)) among the samples anodized by stirring the electrode during anodization. In particular, the lowest values are obtained for the sample anodized under static conditions. In conclusion, the parameter that considerably affects the efficiency of the photocatalysts is the donor density which makes the sample anodized at 1000 rpm a suitable photoanode for photoelectrochemical water splitting.

3.7. Electrochemical Impedance Spectroscopy

Figure 8 shows the Nyquist (a) and b)), Bode-phase (c) and d)) and Bode-modulus (c) and d)) plots at an applied potential of 0.35 V (vs. Ag/AgCl) in both dark and light conditions of the samples anodized at 0, 1000, 2000 and 3000 rpm.

Nyquist plots (Figs. 8 a)-b)) show that under light conditions the impedances of all the samples considerably decrease with respect to those under dark conditions because of the photogenerated charge carriers which reduce charge transfer resistance [12]. Additionally, in both dark and light conditions, the lowest impedance values correspond to the nanostructures anodized at 1000 rpm. This is due to the fact that the morphology of this sample (see Fig. 4) consists of a nanotubular structure with free-entrances of the nanotubes that were accessible to the electrolyte and the generated holes can easily reach them and thus, resistance decreases [59]. Furthermore, under light conditions nanotubes are more accessible to the light and more electron-hole pairs are photogenerated which reduces impedance [12]. On the other hand, the higher impedance values obtained for the rest of the nanostructures (anodized at 0, 2000 and 3000 rpm) are attributed to the morphology of these nanostructures (Fig. 4), i.e. an initiation layer or a collapsed and stacked nanotube layer, which imply that their resistances appreciably increase.

In Bode-phase plots (Figs. 8 c) and d)) two well-differentiated time constants can be elucidated. These two time constants are the result of the superposition of two time constants at low frequencies and another one at high frequencies, suggesting a total of three time constants for the nanostructures. Consequently, the experimental data can be fitted to an electrical equivalent circuit consisting of a resistive element (R_S) and three groups of resistance and constant phase elements (*R-CPE*) as Figure 8 e) shows. Furthermore, the Bode-modulus representations indicate that under illumination the impedance modulus decreases and they also show that the resistance associated with the

electrolyte (R_S, which is the impedance at high frequencies) is similar for all the samples.

Figure 8 e) shows that the electrical equivalent circuit used for the fitting of the experimental data consists of a resistive element (R_S) corresponding to the solution resistance, two groups of resistance and constant phase elements in parallel corresponding to the top and the nanotubular layers (R_1-CPE_1 and R_2-CPE_2, respectively) and another R_3-CPE_3 group that corresponds to the compact layer of iron oxide that remains unchanged beneath the nanostructure after annealing. Constant phase elements have been used instead of pure capacitors to justify frequency dispersion and non-ideality. The resistance values of this equivalent circuit are shown in Table 2. Chi-squared values (χ^2) were calculated in order to determine the suitability of the equivalent circuit fitting. Since all χ^2 are in the order of 10^{-3} the quality of data fitting to the proposed equivalent circuit is proved.

According to Table 2, the resistance values are lower under light conditions than under dark ones because illumination promotes the photogeneration of charge carriers which in turn result in an increase in conductivity. Concerning R_S values, they are similar for all the samples studied (between 2 and 4 $\Omega \cdot cm^2$), since this resistance is associated with the solution resistance, which is the same for all the experiments. R_3 values are the highest in all the samples because this resistance is associated with the compact oxide layer on the bottom of the nanotubular structures, where conductivity is lower. R_2 values are the lowest because these resistances are related to the tubular structure which enhances charge transport and overcome the short hole diffusion length; as a result, conductivity is higher [25]. Finally, R_1 values correspond to the top layer and they are intermediate in comparison to the other resistances associated to the morphology of the samples. In general terms, the values of R_1, R_2 and R_3 are lower for the nanostructure

synthesized at 1000 rpm in comparison to the other ones, especially for the resistances calculated under light conditions (R_1 ~ 2.7 Ω·cm², R_2 ~ 0.3 kΩ·cm², R_3 ~ 2.9 kΩ·cm²). This is related to the intrinsic morphology obtained by stirring the electrode at 1000 rpm (Fig. 4), which offers less resistance.

The results of the EIS are in agreement with the water splitting and stability tests which show that the nanostructure achieving the highest photocurrent density values is the one anodized at 1000 rpm.

3.9. Band gap

The band gap energy was calculated from the measurements of photocurrent density at an applied potential of 0.35 V (vs. Ag/AgCl) at different wavelengths from 300 to 600 nm. The optical band gap can be obtained by Tauc's equation [12,37,60–62]:

$$\alpha \cdot h \cdot \nu = A \cdot (h \cdot \nu - E_g)^n \qquad (\boldsymbol{Eq.8})$$

where α is the absorption coefficient (it can be assumed to be proportional to the photocurrent density i_{ph} [14,63]), $h \cdot \nu$ is the photon energy expressed in eV, A is a constant of the material, E_g is the band gap and n is a constant that depends on the kind of electronic transition. The value of n is equal to ½ for a direct allowed transition and n is equal to 2 for an indirect allowed transition. Thus, a representation of $(\alpha \cdot h \cdot \nu)^2$ vs. photon energy can be used to calculate the direct band gap from the intercept of the linear region of the plot with the x-axis. On the other hand, the indirect band gap can be calculated from the intercept of the linear region of the plot of $(\alpha \cdot h \cdot \nu)^{1/2}$ vs. photon energy with the real axis.

Generally, most of the studies assume an indirect (phonon-assisted) band gap transition for hematite, since their energy bands are parabolic with respect to the crystal momentum. Nevertheless, more recent works consider a direct band gap in hematite that has been attributed to quantum size-effects [9,64,65]. Figure 9 a) shows $(\alpha \cdot h \cdot \nu)^2$ vs. photon energy plots, and the inset shows the E_g values obtained from these plots. It is noticeable that the direct band gaps of all the samples are similar in the range of 2.3 – 2.5 eV, showing no effect of the electrode rotation speed on this parameter. From the $(\alpha \cdot h \cdot \nu)^{1/2}$ vs. photon energy representations (Fig. 9 b)), the indirect band gap energy was calculated, with values in the order of 1.8 - 1.9 eV (see inset of the Figure 9 b)) that are lower than the values of the direct band gap. Therefore, it can be pointed out that there are no differences among the samples which means that the indirect band gap is not affected by the hydrodynamic conditions. Both values of direct and indirect band gap for hematite nanostructures were in agreement with the literature [9,60,66,67]. In general terms, smaller band gap values indicate that a wider solar spectrum fraction will be absorbed generating more electron-hole pairs [9], but for photoelectrochemical water splitting an energy close to ~2 eV is necessary for the charge carriers to have enough energy to split water [9,68–70]. Then, according to the band gap results the synthesized nanostructures are efficient photocatalysts for photoelectrochemical water splitting.

4. Conclusions

In this study, the effect of the controlled hydrodynamic conditions on the formation of iron oxide nanostructures by electrochemical anodization was analyzed. Different rotation speeds (0, 1000, 2000 and 3000 rpm), were tested in order to obtain an efficient nanostructure for being used as photocatalyst for photoelectrochemical water splitting.

The results show that the most appropriated electrode rotation speed in the studied range is 1000 rpm, because it allows obtaining a nanostructure that achieved a photocurrent density of ~0.130 mA · cm^{-2} at 0.54 V (vs. Ag/AgCl) in the photoelectrochemical water splitting tests. FE-SEM images show that this good performance was due to the morphology of this nanostructure which was nanotubular with the entrances of the real tubes accessible to light. These results are in agreement with the EIS measurements that revealed the lowest resistance values for this nanostructure; this suggests that its conductivity is the highest. Mott-Schottky analysis show that the donor density values of the nanostructure anodized at 1000 rpm avoid the growth of defects acting as carrier traps, presenting the higher donor density values when measurements were carried out under light conditions. In summary, iron anodization under controlled hydrodynamic conditions is a novel and effective method to obtain iron oxide nanostructures directly on the metal substrate. In particular, an efficient photocatalyst consisting of a nanotubular structure mainly composed by hematite is obtained by stirring the electrode at 1000 rpm.

Acknowledgements: The authors would like to express their gratitude for the financial support to the Ministerio de Economía y Competitividad (Reference: BES-2014-068713, Project Code: CTQ2013-42494-R), for its help in the Laser Raman Microscope acquisition (UPOV08-3E-012), for the co-finance by the European Social Fund and to Dr. Asunción Jaime for her translation assistance.

REFERENCES

[1] J. Ge, J. Tian, L. Zhuo, H. Chen, B. Tang, Fabrication of self-assembled iron oxide hierarchical nanostructures and their application in water treatment, Solid State Sci. 13 (2011) 1554–1559.

[2] P. Sun, L. You, D. Wang, Y. Sun, J. Ma, G. Lu, Synthesis and gas sensing properties of bundle-like α-Fe_2O_3 nanorods, Sens. Actuators B Chem. 156 (2011) 368–374.

[3] N.M. Rashid, N. Kishi, T. Soga, Effects of nanostructures on iron oxide based dye sensitized solar cells fabricated on iron foils, Mater. Res. Bull. 77 (2016) 126–130.

[4] M. Khosravi, S. Azizian, Synthesis of Fe_3O_4 flower-like hierarchical nanostructures with high adsorption performance toward dye molecules, Colloid Surf. A-Physicochem. Eng. Asp. 482 (2015) 438–446.

[5] N. Sudha, S. Yousuf, E.V.M.V. Israel, M.S. Paulraj, P. Dhanaraj, On the accessibility of surface-bound drugs on magnetic nanoparticles. Encapsulation of drugs loaded on modified dextran-coated superparamagnetic iron oxide by β-cyclodextrin, Colloid Surf. B-Biointerfaces. 141 (2016) 423–428.

[6] S.A. Pervez, D. Kim, U. Farooq, A. Yaqub, J.H. Choi, Y.J. Lee, et al., Crystalline iron oxide nanotube arrays with high aspect ratio as binder free anode for Li-ion batteries, Phys. Status Solidi A-Appl. Mat. 211 (2014) 1889–1894.

[7] L. Jia, K. Harbauer, P. Bogdanoff, K. Ellmer, S. Fiechter, Sputtering Deposition of Ultra-thin α-Fe_2O_3 Films for Solar Water Splitting, J. Mater. Sci. Technol. 31 (2015) 655–659.

[8] L. Wang, C.-Y. Lee, P. Schmuki, Ti and Sn co-doped anodic α-Fe_2O_3 films for efficient water splitting, Electrochem. Commun. 30 (2013) 21–25.

[9] K. Sivula, F. Le Formal, M. Grätzel, Solar Water Splitting: Progress Using Hematite (α-Fe_2O_3) Photoelectrodes, ChemSusChem. 4 (2011) 432–449.

[10] M.F. Al-Kuhaili, M. Saleem, S.M.A. Durrani, Optical properties of iron oxide (α-Fe_2O_3) thin films deposited by the reactive evaporation of iron, J. Alloys Compd. 521 (2012) 178–182.

[11] B.D. Chernomordik, H.B. Russell, U. Cvelbar, J.B. Jasinski, V. Kumar, T. Deutsch, et al., Photoelectrochemical activity of as-grown, α-Fe_2O_3 nanowire array electrodes for water splitting, Nanotechnology. 23 (2012) 194009–194018.

[12] R.R. Rangaraju, A. Panday, K.S. Raja, M. Misra, Nanostructured anodic iron oxide film as photoanode for water oxidation, J. Phys. D-Appl. Phys. 42 (2009) 135303–135313.

[13] S.K. Mohapatra, S.E. John, S. Banerjee, M. Misra, Water Photooxidation by Smooth and Ultrathin α-Fe_2O_3 Nanotube Arrays, Chem. Mat. 21 (2009) 3048–3055.

[14] L. Wang, C.Y. Lee, P. Schmuki, Influence of annealing temperature on photoelectrochemical water splitting of a-Fe_2O_3 films prepared by anodic deposition, Electrochim. Acta. 91 (2013) 307–313.

[15] Z. Zhang, M.F. Hossain, T. Takahashi, Self-assembled hematite (α-Fe_2O_3) nanotube arrays for photoelectrocatalytic degradation of azo dye under simulated solar light irradiation, Appl. Catal. B-Environ. 95 (2010) 423–429.

[16] B. Klahr, S. Gimenez, F. Fabregat-Santiago, T. Hamann, J. Bisquert, Water oxidation at hematite photoelectrodes: The role of surface states, J. Am. Chem. Soc. 134 (2012) 4294–4302.

[17] R.R. Rangaraju, K.S. Raja, a. Panday, M. Misra, An investigation on room temperature synthesis of vertically oriented arrays of iron oxide nanotubes by anodization of iron, Electrochim. Acta. 55 (2010) 785–793.

[18] M. Mishra, D.-M. Chun, α-Fe_2O_3 as a photocatalytic material: A review, Appl. Catal. A-Gen. 498 (2015) 126–141.

[19] S.C. Warren, K. Voïtchovsky, H. Dotan, C.M. Leroy, M. Cornuz, F. Stellacci, et al., Identifying champion nanostructures for solar water-splitting, Nat. Mater. 12 (2013) 842–849.

[20] A. Annamalai, P.S. Shinde, T.H. Jeon, H.H. Lee, H.G. Kim, W. Choi, et al., Fabrication of superior α-Fe_2O_3 nanorod photoanodes through ex-situ Sn-doping for solar water splitting, Sol. Energy Mater. Sol. Cells. 144 (2016) 247–255.

[21] V. a N. De Carvalho, R. a D.S. Luz, B.H. Lima, F.N. Crespilho, E.R. Leite, F.L. Souza, Highly oriented hematite nanorods arrays for photoelectrochemical water splitting, J. Power Sources. 205 (2012) 525–529.

[22] A. Pu, J. Deng, Y. Hao, X. Sun, J. Zhong, Thickness effect of hematite nanostructures prepared by hydrothermal method for solar water splitting, Appl. Surf. Sci. 320 (2014) 213–217.

[23] P.S. Shinde, A. Annamalai, J.H. Kim, S.H. Choi, J.S. Lee, J.S. Jang, Exploiting the dynamic Sn diffusion from deformation of FTO to boost the photocurrent performance of hematite photoanodes, Sol. Energy Mater. Sol. Cells. 141 (2015) 71–79.

[24] K. Xie, J. Li, Y. Lai, W. Lu, Z. Zhang, Y. Liu, et al., Highly ordered iron oxide nanotube arrays as electrodes for electrochemical energy storage, Electrochem. Commun. 13 (2011) 657–660.

[25] S. Grigorescu, C.Y. Lee, K. Lee, S. Albu, I. Paramasivam, I. Demetrescu, et al., Thermal air oxidation of Fe: Rapid hematite nanowire growth and photoelectrochemical water splitting performance, Electrochem. Commun. 23 (2012) 59–62.

[26] K. Xie, M. Guo, H. Huang, Y. Liu, Fabrication of iron oxide nanotube arrays by electrochemical anodization, Corrosion Sci. 88 (2014) 66–75.

[27] C.Y. Lee, L. Wang, Y. Kado, R. Kirchgeorg, P. Schmuki, Si-doped Fe_2O_3 nanotubular/nanoporous layers for enhanced photoelectrochemical water splitting, Electrochem. Commun. 34 (2013) 308–311.

[28] Y. Konno, E. Tsuji, P. Skeldon, G.E. Thompson, H. Habazaki, Factors influencing the growth behaviour of nanoporous anodic films on iron under galvanostatic anodizing, J. Solid State Electrochem. 16 (2012) 3887–3896.

[29] S.P. Albu, A. Ghicov, P. Schmuki, High aspect ratio, self-ordered iron oxide nanopores formed by anodization of Fe in ethylene glycol/NH_4F electrolytes, Phys. Status Solidi - Rapid Res. Lett. 3 (2009) 64–66.

[30] H.E. Prakasam, O.K. Varghese, M. Paulose, G.K. Mor, C. a Grimes, Synthesis and photoelectrochemical properties of nanoporous iron (III) oxide by potentiostatic anodization, Nanotechnology. 17 (2006) 4285–4291.

[31] B. Sarma, A.L. Jurovitzki, Y.R. Smith, R.S. Ray, M. Misra, Influence of annealing temperature on the morphology and the supercapacitance behavior of iron oxide nanotube (Fe-NT), J. Power Sources. 272 (2014) 766–775.

[32] R. Sánchez-Tovar, R.M. Fernández-Domene, D.M. García-García, J. García-Antón, Enhancement of photoelectrochemical activity for water splitting by controlling hydrodynamic conditions on titanium anodization, J. Power Sources. 286 (2015) 224–231.

[33] R.M. Fernández-Domene, R. Sánchez-Tovar, B. Lucas-Granados, J. García-Antón, Improvement in photocatalytic activity of stable WO_3 nanoplatelet globular clusters arranged in a tree-like fashion: Influence of rotation velocity during anodization, Appl. Catal. B-Environ. 189 (2016) 266–282.

[34] R. Sánchez-Tovar, R.M. Fernández-Domene, M.T. Montañés, A. Sanz-Marco, J. Garcia-Antón, ZnO/ZnS heterostructures for hydrogen production by photoelectrochemical

water splitting, RSC Adv. 6 (2016) 30425–30435.

[35] B. Lucas-Granados, R. Sánchez-Tovar, R.M. Fernández-Domene, J. García-Antón, Study of the annealing conditions and photoelectrochemical characterization of a new iron oxide bi-layered nanostructure for water splitting, Sol. Energy Mater. Sol. Cells. 153 (2016) 68–77.

[36] G. Rahman, O.-S. Joo, Photoelectrochemical water splitting at nanostructured α-Fe_2O_3 electrodes, Int. J. Hydrog. Energy. 37 (2012) 13989–13997.

[37] M.M. Momeni, Y. Ghayeb, F. Mohammadi, Solar water splitting for hydrogen production with Fe_2O_3 nanotubes prepared by anodizing method: effect of anodizing time on performance of Fe_2O_3 nanotube arrays, J. Mater. Sci.-Mater. Electron. 26 (2014) 685–692.

[38] K. Yasuda, P. Schmuki, Control of morphology and composition of self-organized zirconium titanate nanotubes formed in $(NH_4)_2SO_4/NH_4F$ electrolytes, Electrochim. Acta. 52 (2007) 4053–4061.

[39] J.M. Macak, H. Hildebrand, U. Marten-Jahns, P. Schmuki, Mechanistic aspects and growth of large diameter self-organized TiO_2 nanotubes, J. Electroanal. Chem. 621 (2008) 254–266.

[40] A.M. Jubb, H.C. Allen, Vibrational spectroscopic characterization of hematite, maghemite, and magnetite thin films produced by vapor deposition, ACS Appl. Mater. Interfaces. 2 (2010) 2804–2812.

[41] T. Sharifi, E. Gracia-Espino, H.R. Barzegar, X. Jia, F. Nitze, G. Hu, et al., Formation of nitrogen-doped graphene nanoscrolls by adsorption of magnetic γ-Fe_2O_3 nanoparticles., Nat. Commun. 4 (2013) 2319–2328.

[42] D.L. a de Faria, F.N. Lopes, Heated goethite and natural hematite: Can Raman spectroscopy be used to differentiate them?, Vib. Spectrosc. 45 (2007) 117–121.

[43] S. Nie, E. Starodub, M. Monti, D. a. Siegel, L. Vergara, F. El Gabaly, et al., Insight into magnetite's redox catalysis from observing surface morphology during oxidation, J. Am. Chem. Soc. 135 (2013) 10091–10098.

[44] M. Lübbe, A.M. Gigler, R.W. Stark, W. Moritz, Identification of iron oxide phases in thin films grown on Al_2O_3(0001) by Raman spectroscopy and X-ray diffraction, Surf. Sci. 604 (2010) 679–685.

[45] P. Roy, S.P. Albu, P. Schmuki, TiO_2 nanotubes in dye-sensitized solar cells: Higher efficiencies by well-defined tube tops, Electrochem. Commun. 12 (2010) 949–951.

[46] J. Borràs-Ferrís, R. Sánchez-Tovar, E. Blasco-Tamarit, R.M. Fernández-Domene, J. García-Antón, Effect of Reynolds number and lithium cation insertion on titanium anodization, Electrochim. Acta. 196 (2016) 24–32.

[47] C.-Y. Lee, L. Wang, Y. Kado, M.S. Killian, P. Schmuki, Anodic nanotubular/porous hematite photoanode for solar water splitting: substantial effect of iron substrate purity., ChemSusChem. 7 (2014) 934–40.

[48] H.-J. Ahn, M.-J. Kwak, J.-S. Lee, K.-Y. Yoon, J.-H. Jang, Nanoporous hematite structures to overcome short diffusion lengths in water splitting, J. Mater. Chem. A. 2 (2014) 19999–20003.

[49] A. Mettenbörger, T. Singh, A.P. Singh, T.T. Järvi, M. Moseler, M. Valldor, et al., Plasma-chemical reduction of iron oxide photoanodes for efficient solar hydrogen production, Int. J. Hydrog. Energy. 39 (2014) 4828–4835.

[50] L.M. Peter, K.G.U. Wijayantha, A.A. Tahir, Kinetics of light-driven oxygen evolution at α-Fe_2O_3 electrodes, Faraday Discuss. 155 (2012) 309–322.

[51] P. Dias, A. Vilanova, T. Lopes, L. Andrade, A. Mendes, Extremely Stable Bare Hematite Photoanode for Solar Water Splitting, Nano Energy. 23 (2016) 70–79.

[52] K. Gelderman, L. Lee, S.W. Donne, Flat-Band Potential of a Semiconductor : Using the Mott – Schottky Equation, J. Chem. Educ. 84 (2007) 685–688.

[53] S.S. Shinde, R.A. Bansode, C.H. Bhosale, K.Y. Rajpure, Physical properties of hematite α-Fe_2O_3 thin films: application to photoelectrochemical solar cells, J. Semicond. 32 (2011) 013001–013009.

[54] F. V. Herrera, P. Grez, R. Schrebler, L.A. Ballesteros, E. Muñoz, R. Córdova, et al., Preparation and Photoelectrochemical Characterization of Porphyrin-Sensitized α-Fe_2O_3 Thin Films, J. Electrochem. Soc. 157 (2010) D302–D308.

[55] S. Shen, J. Zhou, C.-L. Dong, Y. Hu, E.N. Tseng, P. Guo, et al., Surface Engineered Doping of Hematite Nanorod Arrays for Improved Photoelectrochemical Water Splitting, Sci. Rep. 4 (2014) 6627–6636.

[56] I. Cesar, K. Sivula, A. Kay, R. Zboril, M. Grätzel, Influence of Feature Size, Film Thickness, and Silicon Doping on the Performance of Nanostructured Hematite Photoanodes for Solar Water Splitting, J. Phys. Chem. C. 113 (2009) 772–782.

[57] D. Wang, X. Zhang, P. Sun, S. Lu, L. Wang, C. Wang, et al., Photoelectrochemical water

splitting with rutile TiO_2 nanowires array: Synergistic effect of hydrogen treatment and surface modification with anatase nanoparticles, Electrochim. Acta. 130 (2014) 290–295.

[58] M. Radecka, M. Rekas, A. Trenczek-Zajac, K. Zakrzewska, Importance of the band gap energy and flat band potential for application of modified TiO_2 photoanodes in water photolysis, J. Power Sources. 181 (2008) 46–55.

[59] A.G. Tamirat, J. Rick, A.A. Dubale, W.-N. Su, B.-J. Hwang, Using hematite for photoelectrochemical water splitting: a review of current progress and challenges, Nanoscale Horiz. 1 (2016) 243-267.

[60] H. Jun, B. Im, J.Y. Kim, Y.-O. Im, J.-W. Jang, E.S. Kim, et al., Photoelectrochemical water splitting over ordered honeycomb hematite electrodes stabilized by alumina shielding, Energy Environ. Sci. 5 (2012) 6375–6382.

[61] Z. Zhang, M.F. Hossain, T. Takahashi, Fabrication of shape-controlled a-Fe_2O_3 nanostructures by sonoelectrochemical anodization for visible light photocatalytic application, Mater. Lett. 64 (2010) 435–438.

[62] S. Konar, H. Kalita, N. Puvvada, S. Tantubay, M.K. Mahto, S. Biswas, et al., Shape-dependent catalytic activity of CuO nanostructures, J. Catal. 336 (2016) 11–22.

[63] J.H. Park, S. Kim, A.J. Bard, Novel carbon-doped TiO_2 nanotube arrays with high aspect ratios for efficient solar water splitting, Nano Lett. 6 (2006) 24–28.

[64] K. Sivula, R. Zboril, F. Le Formal, R. Robert, A. Weidenkaff, J. Tucek, et al., Photoelectrochemical Water Splitting with Mesoporous Hematite Prepared by a Solution-Based Colloidal Approach Photoelectrochemical Water Splitting with Mesoporous Hematite Prepared by a Solution-Based Colloidal Approach, J. Am. Chem. Soc. 132 (2010) 7436–7444.

[65] B.L. Vayssieres, C. Sathe, S.M. Butorin, D.K. Shuh, J. Nordgren, J. Guo, One-Dimensional Quantum- Confinement Effect in a -Fe_2O_3 Ultrafine Nanorod Arrays, Adv. Mater. 17 (2005) 2320–2323.

[66] T. Mushove, T.M. Breault, L.T. Thompson, Synthesis and characterization of hematite nanotube arrays for photocatalysis, Ind. Eng. Chem. Res. 54 (2015) 4285–4292.

[67] P. Mallick, B.N. Dash, X-ray Diffraction and UV-Visible Characterizations of α-Fe_2O_3 Nanoparticles Annealed at Different Temperature, Nanosci. Nanotechnol. 3 (2013) 130–134.

[68] J.Y. Kim, G. Magesh, D.H. Youn, J.-W. Jang, J. Kubota, K. Domen, et al., Single-crystalline,

wormlike hematite photoanodes for efficient solar water splitting, Sci. Rep. 3 (2013) 2681–2689.

[69] A.B. Murphy, Band-gap determination from diffuse reflectance measurements of semiconductor films, and application to photoelectrochemical water-splitting, Sol. Energy Mater. Sol. Cells. 91 (2007) 1326–1337.

[70] Y. Lin, G. Yuan, S. Sheehan, S. Zhou, D. Wang, Hematite-based solar water splitting: challenges and opportunities, Energy Environ. Sci. 4 (2011) 4862–4869.

FIGURE CAPTIONS

Figure 1. Illustration of the electrode configuration during the electrochemical anodization.

Figure 2. Current density vs. time measurements during anodization of iron at 50 V for 15 minutes in an ethylene glycol solution containing 0.1 M NH_4F and 3 vol% H_2O at the different rotation speeds (0, 1000, 2000 and 3000 rpm).

Figure 3. Raman spectra of the nanostructures obtained by anodization at 50 V for 15 minutes in an ethylene glycol solution containing 0.1 M NH_4F and 3 vol% H_2O at the different rotation speeds (0, 1000, 2000 and 3000 rpm) and annealed in argon during 1 h.

Figure 4. FE-SEM images of the nanostructures obtained by anodization at the different rotation speeds (0, 1000, 2000 and 3000 rpm).

Figure 5. Thickness of the anodized nanostructures as a function of the electrode rotation speed (0, 1000, 2000 and 3000 rpm).

Figure 6. a) Photocurrent density vs. potential measurements obtained by applying chopped light irradiation under simulated 1.5 AM illumination in 1 M KOH for the samples synthesized at the different rotation speeds (0, 1000, 2000 and 3000 rpm). b) Photocurrent density vs. time measurements at an applied potential of 0.35 V (vs. Ag/AgCl) in 1 M KOH during 1 h under simulated 1.5 AM illumination obtained for the samples synthesized at the different rotation speeds (0, 1000, 2000 and 3000 rpm).

Figure 7. Mott-Schottky plots of the samples synthesized at the different rotation speeds (0, 1000, 2000 and 3000 rpm), obtained under dark (a)) and light (b)) conditions in 1 M KOH. Simulated AM 1.5 illumination was used for the light conditions.

Figure 8. Nyquist plots under dark (a)) and light (b)) conditions, and Bode-phase and Bode-modulus plots under dark (c)) and light (d)) conditions, obtained at an applied potential of 0.35 V (vs. Ag/AgCl) in 1 M KOH for the samples anodized at the different rotation speeds (0, 1000, 2000 and 3000 rpm). Simulated AM 1.5 illumination was used for light conditions. e) Electrical equivalent circuit used to simulate the experimental EIS data obtained for the synthesized nanostructures.

Figure 9. a) $(i_{ph} \cdot h \cdot \nu)^2$ vs. photon energy plots for the direct band gap determination for the samples synthesized at the different rotation speeds (0, 1000, 2000 and 3000 rpm). b) $(i_{ph} \cdot h \cdot \nu)^{1/2}$ vs. photon energy plots for the indirect band gap determination for the samples synthesized at the different rotation speeds (0, 1000, 2000 and 3000 rpm).

Figure 1

1. *Rotation Disk Electrode (RDE)*
2. *Motor controller*
3. *Electrochemical cell*
4. *Iron rod (working electrode)*
5. *Platinum foil (counter electrode)*
6. *Power source*
7. *Multimeter*

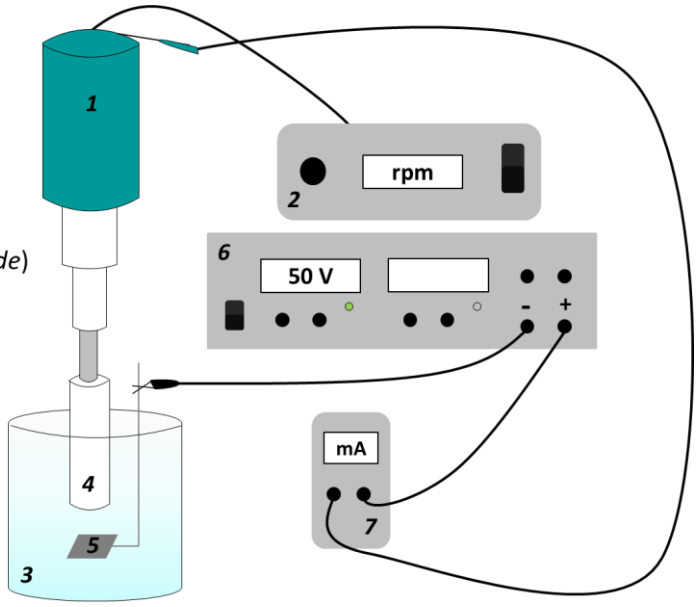

Figure 2

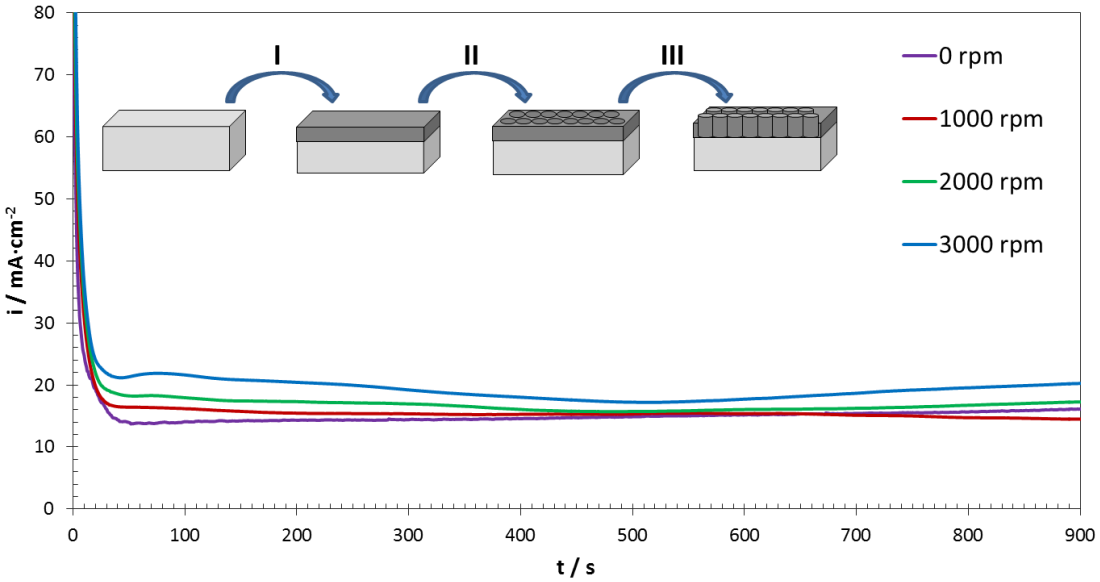
I
II
III
0 rpm
1000 rpm
2000 rpm
3000 rpm
i / mA·cm-2
t / s
0
10
20
30
40
50
60
70
80
0
100
200
300
400
500
600
700
800
900

Figure 3

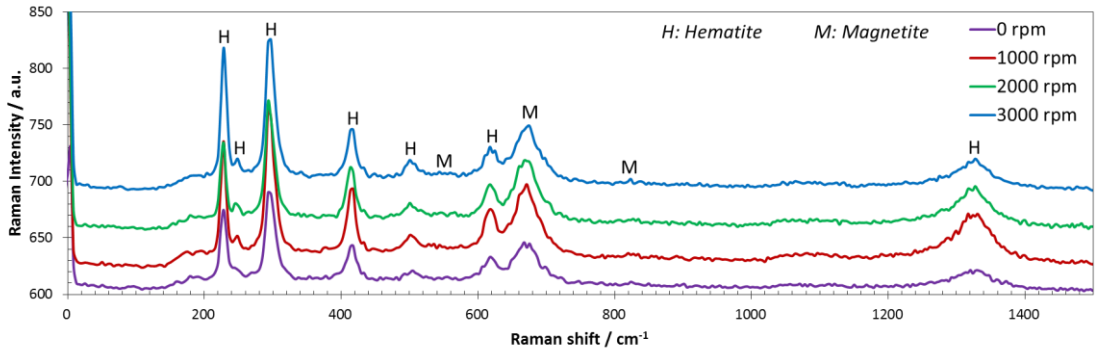
H: Hematite
M: Magnetite
0 rpm
1000 rpm
2000 rpm
3000 rpm
Raman Intensity / a.u.
Raman shift / cm-1
850
800
750
700
650
600
0
200
400
600
800
1000
1200
1400
H
H
H
H
H
M
H
M
M
H

Figure 4

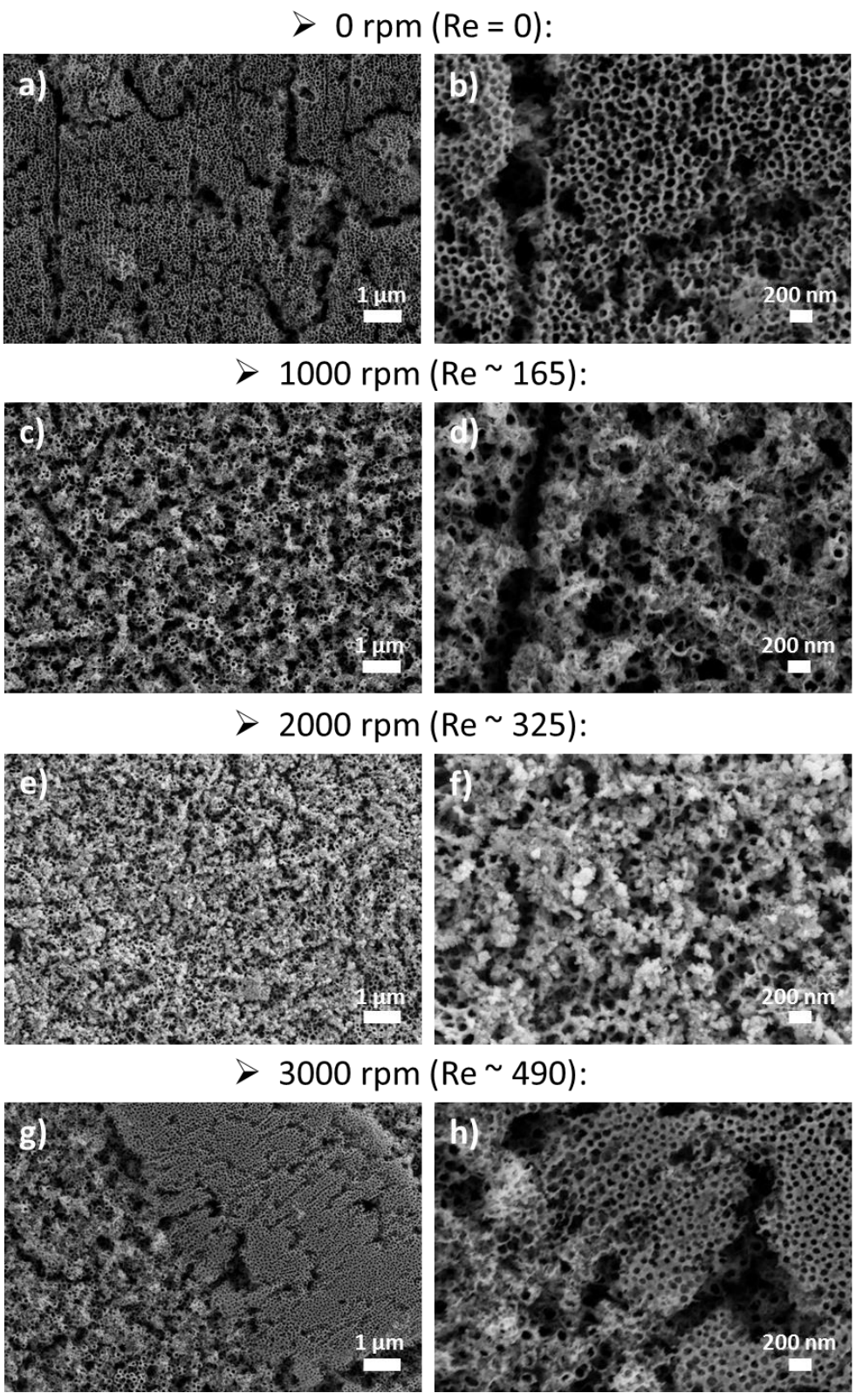
➢ 0 rpm (Re = 0):
a)
1 µm
b)
200 nm
➢ 1000 rpm (Re ~ 165):
c)
1 µm
d)
200 nm
➢ 2000 rpm (Re ~ 325):
e)
1 µm
f)
200 nm
➢ 3000 rpm (Re ~ 490):
g)
1 µm
h)
200 nm

Figure 5

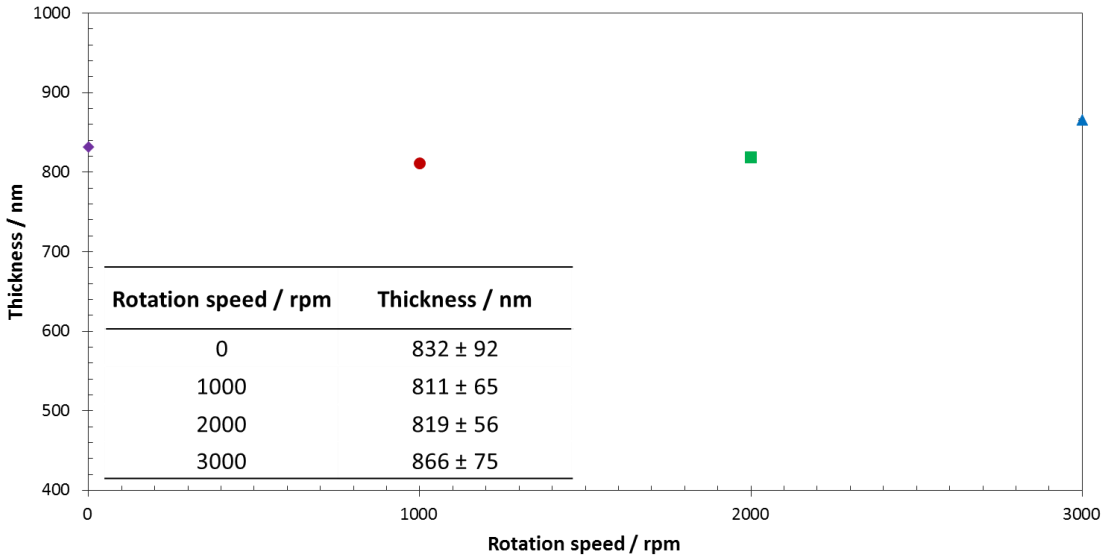

Rotation speed / rpm	Thickness / nm
0	832 ± 92
1000	811 ± 65
2000	819 ± 56
3000	866 ± 75

Figure 6

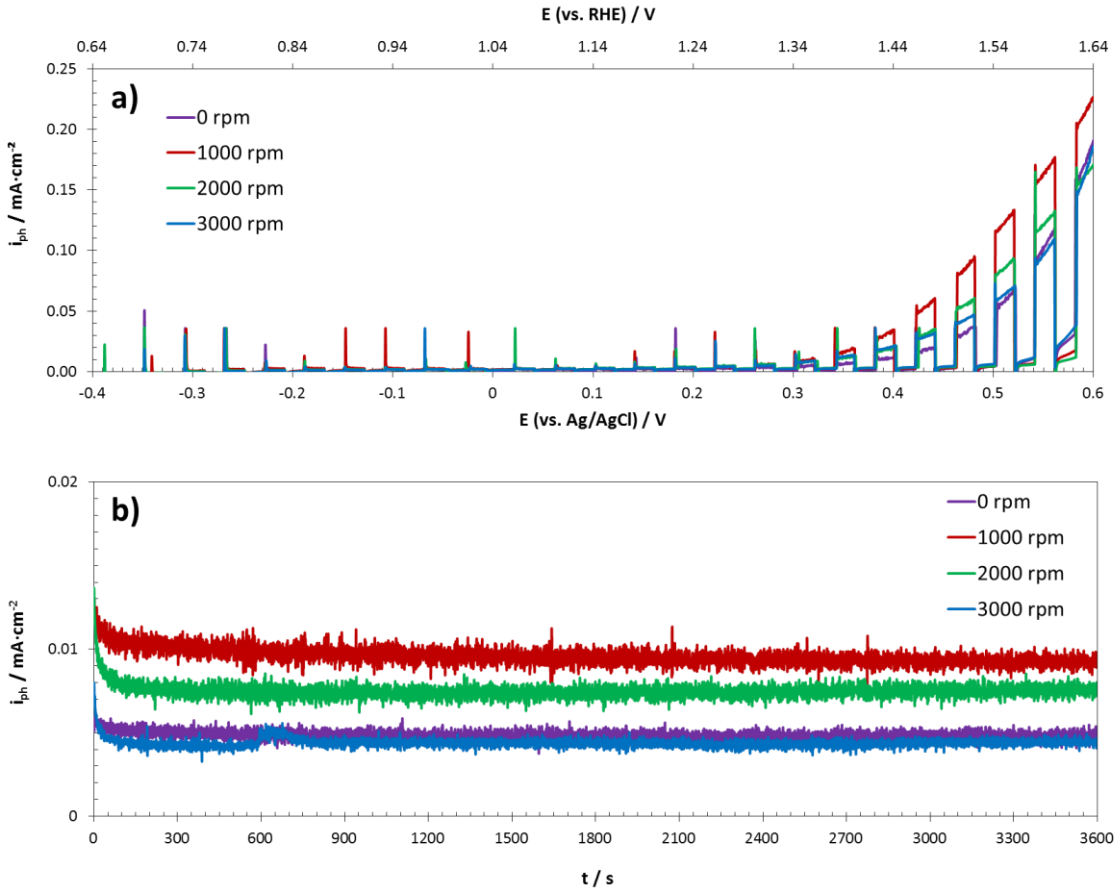
E (vs. RHE) / V
0.64
0.74
0.84
0.94
1.04
1.14
1.24
1.34
1.44
1.54
1.64
a)
0 rpm
1000 rpm
2000 rpm
3000 rpm
i_ph / mA·cm⁻²
0.25
0.20
0.15
0.10
0.05
0.00
-0.4
-0.3
-0.2
-0.1
0
0.1
0.2
0.3
0.4
0.5
0.6
E (vs. Ag/AgCl) / V
b)
0 rpm
1000 rpm
2000 rpm
3000 rpm
i_ph / mA·cm⁻²
0.02
0.01
0
0
300
600
900
1200
1500
1800
2100
2400
2700
3000
3300
3600
t / s

Figure 7

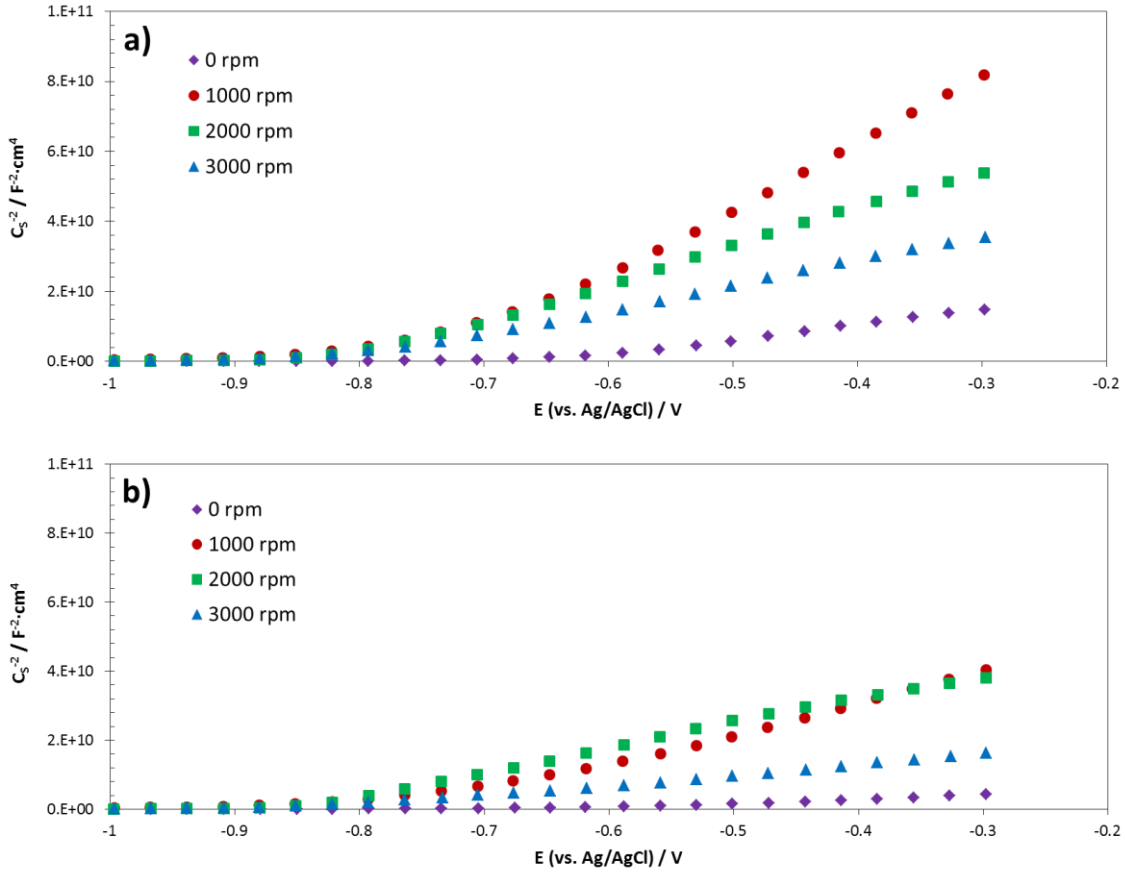
a)
0 rpm
1000 rpm
2000 rpm
3000 rpm
C_S^{-2} / F^{-2}·cm^4
1.E+11
8.E+10
6.E+10
4.E+10
2.E+10
0.E+00
-1
-0.9
-0.8
-0.7
-0.6
-0.5
-0.4
-0.3
-0.2
E (vs. Ag/AgCl) / V
b)
0 rpm
1000 rpm
2000 rpm
3000 rpm
C_S^{-2} / F^{-2}·cm^4
1.E+11
8.E+10
6.E+10
4.E+10
2.E+10
0.E+00
-1
-0.9
-0.8
-0.7
-0.6
-0.5
-0.4
-0.3
-0.2
E (vs. Ag/AgCl) / V

Figure 8

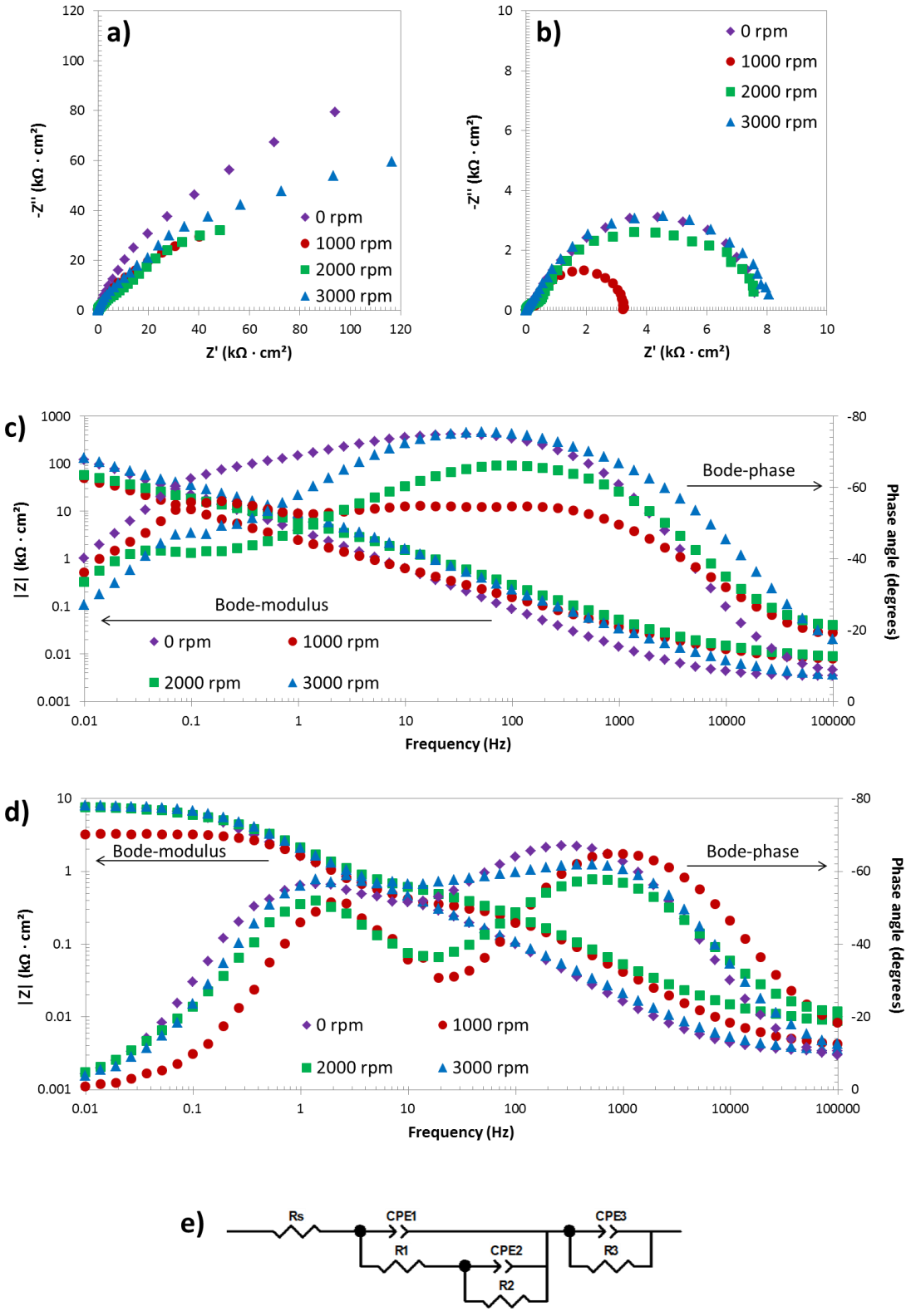
a)
-Z'' (kΩ · cm²)
Z' (kΩ · cm²)
0 rpm
1000 rpm
2000 rpm
3000 rpm
b)
-Z'' (kΩ · cm²)
Z' (kΩ · cm²)
0 rpm
1000 rpm
2000 rpm
3000 rpm
c)
|Z| (kΩ · cm²)
Phase angle (degrees)
Bode-phase
Bode-modulus
0 rpm
1000 rpm
2000 rpm
3000 rpm
Frequency (Hz)
d)
|Z| (kΩ · cm²)
Phase angle (degrees)
Bode-modulus
Bode-phase
0 rpm
1000 rpm
2000 rpm
3000 rpm
Frequency (Hz)
e)
Rs
CPE1
R1
CPE2
R2
CPE3
R3

Figure 9

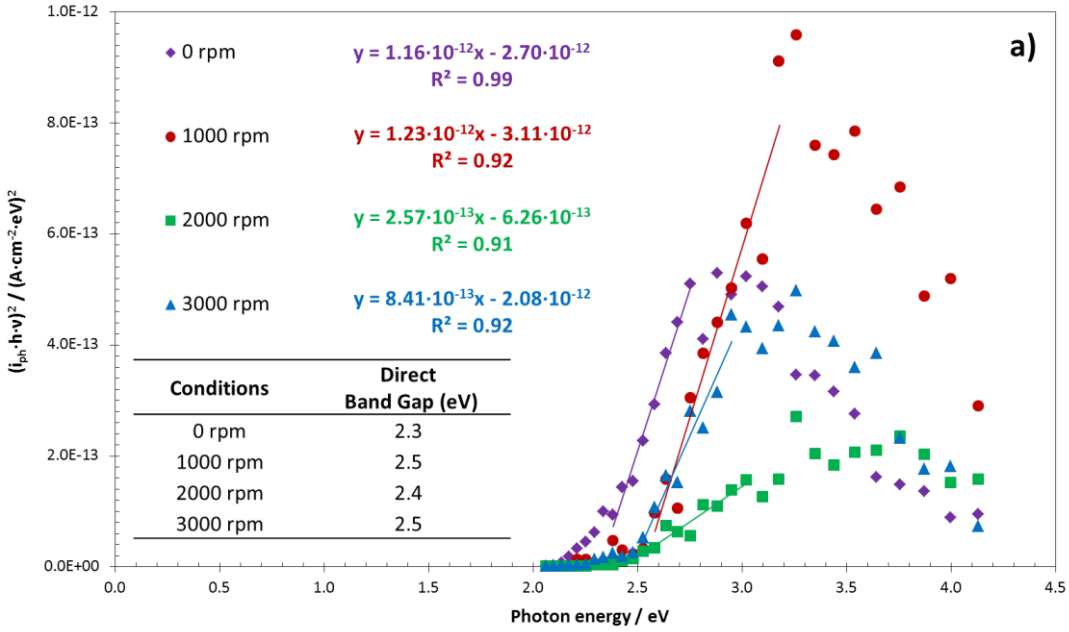
a)
0 rpm
y = 1.16·10-12x - 2.70·10-12
R² = 0.99
1000 rpm
y = 1.23·10-12x - 3.11·10-12
R² = 0.92
2000 rpm
y = 2.57·10-13x - 6.26·10-13
R² = 0.91
3000 rpm
y = 8.41·10-13x - 2.08·10-12
R² = 0.92
Conditions
Direct Band Gap (eV)
0 rpm 2.3
1000 rpm 2.5
2000 rpm 2.4
3000 rpm 2.5
(iph·h·ν)² / (A·cm-²·eV)²
Photon energy / eV

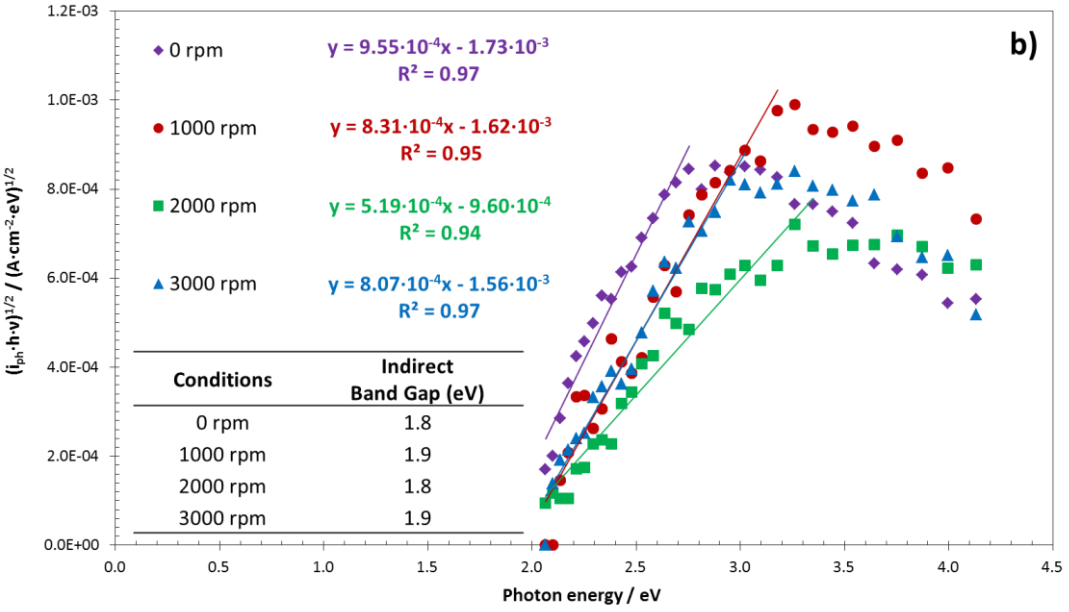
b)
0 rpm
y = 9.55·10-4x - 1.73·10-3
R² = 0.97
1000 rpm
y = 8.31·10-4x - 1.62·10-3
R² = 0.95
2000 rpm
y = 5.19·10-4x - 9.60·10-4
R² = 0.94
3000 rpm
y = 8.07·10-4x - 1.56·10-3
R² = 0.97
Conditions
Indirect Band Gap (eV)
0 rpm 1.8
1000 rpm 1.9
2000 rpm 1.8
3000 rpm 1.9
(iph·h·ν)1/2 / (A·cm-²·eV)1/2
Photon energy / eV

Table 1. Values of donor density (N_D) and flat band potential (E_{FB}) for the samples anodized at the different rotation speeds (0, 1000, 2000 and 3000 rpm), obtained under dark and light conditions in 1 M KOH. Simulated AM 1.5 illumination was used for the light conditions.

Rotation speed / rpm	Conditions	N_D ($\cdot 10^{19}$) / cm^{-3}	E_{FB} (vs. Ag/AgCl) / V
0 rpm	Dark	3.98 ± 1.02	-0.64 ± 0.05
	Light	14.35 ± 3.55	-0.63 ± 0.05
1000 rpm	Dark	1.02 ± 0.24	-0.76 ± 0.04
	Light	2.22 ± 0.66	-0.78 ± 0.03
2000 rpm	Dark	1.64 ± 0.65	-0.80 ± 0.08
	Light	2.44 ± 0.34	-0.85 ± 0.09
3000 rpm	Dark	2.47 ± 0.99	-0.80 ± 0.03
	Light	5.80 ± 0.69	-0.82 ± 0.03

Table 2. Equivalent circuit resistance values for the samples anodized at the different rotation speeds (0, 1000, 2000 and 3000 rpm), obtained under dark and light conditions in 1 M KOH. Simulated AM 1.5 illumination was used for the light conditions.

Conditions	R_S / Ω·cm²	R_1 / Ω·cm²	R_2 / kΩ·cm²	R_3 / kΩ·cm²	χ^2 ($\cdot 10^{-3}$)
Dark					
0 rpm	3.3 ± 0.5	120.0 ± 8.1	5.5 ± 0.7	154.9 ± 20.0	2.5
1000 rpm	4.3 ± 0.5	12.2 ± 2.6	3.0 ± 0.2	63.0 ± 0.5	1.7
2000 rpm	3.0 ± 0.4	7.5 ± 0.3	6.6 ± 0.1	119.7 ± 0.4	0.2
3000 rpm	3.2 ± 0.3	9.6 ± 6.4	7.8 ± 0.1	147.5 ± 8.7	3.4
Light					
0 rpm	3.2 ± 0.9	100 ± 21.8	0.5 ± 0.2	7.6 ± 0.5	0.6
1000 rpm	3.0 ± 0.4	2.7 ± 0.1	0.3 ± 0.1	2.9 ± 0.8	0.6
2000 rpm	2.8 ± 0.9	8.0 ± 0.3	0.4 ± 0.1	7.3 ± 0.5	0.7
3000 rpm	2.1 ± 1.0	4.5 ± 3.0	0.9 ± 0.3	7.4 ± 0.2	0.3